Analytical Methods

Accepted Manuscript

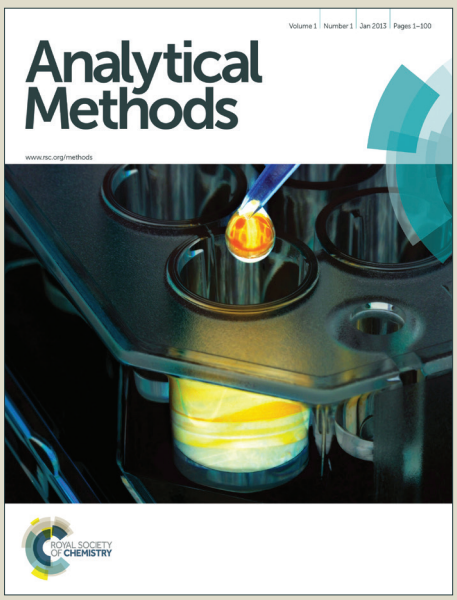

This is an *Accepted Manuscript*, which has been through the Royal Society of Chemistry peer review process and has been accepted for publication.

Accepted Manuscripts are published online shortly after acceptance, before technical editing, formatting and proof reading. Using this free service, authors can make their results available to the community, in citable form, before we publish the edited article. We will replace this *Accepted Manuscript* with the edited and formatted *Advance Article* as soon as it is available.

You can find more information about *Accepted Manuscripts* in the Information for Authors.

Please note that technical editing may introduce minor changes to the text and/or graphics, which may alter content. The journal's standard Terms & Conditions and the Ethical guidelines still apply. In no event shall the Royal Society of Chemistry be held responsible for any errors or omissions in this *Accepted Manuscript* or any consequences arising from the use of any information it contains.

ROYAL SOCIETY OF CHEMISTRY

www.rsc.org/methods

Catalytic activity for CO oxidation of Cu-CeO_2 composite nanoparticles synthesized by a hydrothermal method

Yuxiu Li [a], Yun Cai [a], Xinxin Xing [a], Nan Chen [b], Dongyang Deng [a], Yude Wang [a,c*]

a *Department of Materials Science and Engineering, Yunnan University, 650091 Kunming, Peoples' Republic of China*

b *Department of Physics, Yunnan University, 650091 Kunming, Peoples' Republic of China*

c *Yunnan Province Key Lab of Mico-Nano Materials and Technology*, *Yunnan University, 650091 Kunming, People's Republic of China*

[*] To whom correspondence should be addressed. Fax: +86-871-65153832; Tel: +86-871-65031124; E-mail: ydwang@ynu.edu.cn

Abstract:

A facile hydrothermal method has been developed for the synthesis of nanosized Cu-CeO_2 composites with various Cu contents. The obtained catalysts, with Cu/CeO_2 atomic ratio in the range 0–40%, were characterized as to their structure, morphology, and redox features by the X-ray diffraction, scanning electron microscope, transmission electron microscopy, N_2 physisorption, and temperature programmed reduction with hydrogen. The experimental results show that the particles are the high crystalline CeO_2 nanopowders of 5-8 nm primary particle size and the Cu nanoparticles are indeed coexisted with the CeO_2 nanoparticles (cubic fluorite CeO_2). The influence of Cu contents on their catalytic performance for the CO oxidation was also studied. As for catalytic reactivity, nanosized Cu-CeO_2 composites have a higher catalytic activity than CeO_2 in CO oxidation. It is ascribed to the effect between the cycle transition of Ce^{4+}/Ce^{3+}, oxygen vacancies and surface area, which are induced by copper. The catalytic activity of the Cu-CeO_2 composites exhibits Cu content dependence where the best catalytic activity occurs on Cu/CeO_2 atomic ratio of 30%. In addition, nanosized Cu-CeO_2 composites also show high catalytic activity for selective oxidation of CO in excess H_2 at relatively low temperature.

Keywords: Hydrothermal synthesis; Cu-CeO_2 composites; Nanoparticles; CO oxidation

1. Introduction

Cerium dioxide (CeO_2) has attracted considerable attention in recent years, owing to its broad range of applications in various fields, ranging from catalysis to ceramics, fuel cell technologies, gas sensors, solid state electrolytes, ceramic biomaterials, and so on [1]. Particularly, the applications of CeO_2 in environmental catalysis have shown great potential and been found to be effective in the promotion of catalytic reactions for CO oxidation [2]. As an excellent catalytic material, the most important property of CeO_2 material is its oxygen storage and release capacity (OSC) via the redox shift between Ce^{4+} and Ce^{3+} under oxidizing and reducing conditions, respectively [3,4]. The redox and catalytic properties of ceria are also dependent upon some other factors, including particle size, phase modification, structural lattice defects, and chemical nonstoichiometry. For a catalyst, the particle size in nanometer scale results in increasing the specific surface area and changing its morphology, thus providing a larger number of more reactive edge sites as well as better catalytic performance. Therefore, nanostructured CeO_2 materials with the different morphologies for CO oxidation have been widely investigated in the last decade [2,5-8]. Various nanostructures of CeO_2, such as nanoparticles [9], nanotubes [10], nanowires [9,10], nanorods [9-11], nanocubes [12], nanospindle-like [13], and porous structures [14,15] have been prepared with alternative approaches including wet chemical methods such as sol-gel and hydrothermal syntheses, and used as a catalyst for CO oxidation.

In spite of the interesting catalytic application, the CeO_2 is not a promising candidate for catalytic samples mainly due to its low catalytic activities [16]. The reduction behavior of ceria can be dramatically changed by the addition of a small amount of Pt, Pd, Au noble

metals or base metals and transition metals [17-21]. Although the addition of noble metals improves the activity and the stability of air and temperature, their high cost may limit their application. Numerous reports have shown that the activity of ceria in total oxidation reactions is greatly enhanced by transitional metals like copper, which is comparable or superior to noble metal catalysts for the preferential oxidation of CO in excess hydrogen [22-24]. Based on the synergism of the redox properties of the system, the promoting effect can be achieved by the formation of copper (or copper oxide)–ceria interactions because of both components being significantly more readily reduced or oxidized than the corresponding independent components [25]. CuO/CeO_2 catalysts exhibit promising properties in terms of activity for CO oxidation [3,26-29]. Cu-modified, deposited, or doped cerium oxide materials have been investigated for CO oxidation and shown high catalytic activities [30-32].

In heterogeneous catalysis, it is well known using wet-chemical routes to synthesis oxide-supported metal catalysts. The preparation conditions have a great effect on the structure of oxide-supported metal catalysts and catalytic performance. On the other hand, recent contributions have shown that the use of nanostructured configurations of the cerium oxide component can provide new catalytic properties [33]. The aim of the present study is to obtain the nanosized $Cu\text{-}CeO_2$ composites with the different Cu contents synthesized by a hydrothermal method and test their catalytic performance for the CO oxidation reaction. In the present work, we investigate the influence of Cu^{2+}/ Ce^{3+} molar ratio on the structure, component, and catalytic performance of nanosized $Cu\text{-}CeO_2$ composites. Catalytic CO oxidation is used as a probing reaction, and the catalyst structures are characterized by a

variety of techniques such as N_2 physisorption, XRD, TEM, TPR, and XPS to understand the relationship between structure, component, and catalytic activity.

2. Material and methods

2.1 Preparation of Cu-CeO_2 composite nanoparticles.

All chemical reagents used in the experiments were obtained from commercial sources as guaranteed-grade reagents and used without further purification. The nanosized Cu-CeO_2 composites with different copper contents were synthesized using copper(II) chloride ($CuCl_2$, 99.9%, Aldrich), NaOH (purity>99.9%) and cerium(III) nitrate hexahydrate ($Ce(NO_3)_3 \cdot 6H_2O$, 99.9%, Aldrich).

In the process, the synthetic procedures were as follows: The 0.868 g cerium(III) nitrate hexahydrate ($Ce(NO_3)_3 \cdot 6H_2O$) were mixed with deionized water (10 mL) with stirring until a homogenous solution was obtained. Required concentration of copper chloride ($CuCl_2$) solution (5 mL) was mixed into the $Ce(NO_3)_3 \cdot 6H_2O$ solution with a Cu^{2+}/ Ce^{3+} molar ratio of 0, 0.05, 0.10, 0.20, 0.30 and 0.40, respectively. After stirring for 10 min, appropriate amount of the mixing solution was dribbled into 10 M NaOH solution (35 mL) and then 10 mL ethylene glycol ($C_2H_6O_2$) was added into the reaction mixture. After stirring for 30 min, the mixed solution was transferred into an autoclave (Parr acid digestion bombs, Teflon cups with 80 mL inner volume). The reactions were performed at 120 ^oC in the autoclaves, respectively. After the elapsed reaction time, the autoclaves were taken out from the oven and left to cool-down spontaneously to the room temperature. The resulting suspensions were centrifuged, and the precipitate was thoroughly washed with ethanol and then dried at 60 ^oC in vacuum drier overnight. The as-prepared samples in subsequent discussions of this

paper are designated as CeO_2, 5Cu-CeO_2, 10Cu-CeO_2, 20Cu-CeO_2, 30Cu-CeO_2, and 40Cu-CeO_2, respectively.

2.2 Characterization.

Powder X-ray diffraction (XRD) data were recorded with a Rigaku D/MAX-3B powder diffractometer using the copper target and k_α radiation (λ = 1.54056 Å). The samples were scanned from 20° to 90° (2θ) in steps of 0.02°. The morphology was observed using scanning electron microscopy (SEM) taken on FEI QUANTA200 with microscope operating at 30 kV. Fourier transformed infrared (FTIR) spectra, in the range of 4000-400 cm^{-1}, were recorded on Perkin Elmer Spectrum GX infrared spectrophotometer. Transmission electron microscopy (TEM) measurement was performed on a Zeiss EM 912Ω instrument at an acceleration voltage of 120 kV, while high-resolution transmission electron microscopy (HRTEM) characterization was done using JEOL JEM-2010 Electron Microscope (with an acceleration voltage of 200 kV). The samples for TEM were prepared by dispersing the final samples in distilled deionized water; this dispersion was then dropped on carbon-copper grids coated by an amorphous carbon film. N_2 adsorption-desorption isotherms at 77 K were recorded on a Micromeritics ASAP 2010 automated sorption analyzer. The samples were outgassed at 150 °C for 20 h before the sorption analysis. X-ray photoelectron spectroscopy (XPS) was carried out at room temperature in ESCALAB 250 system. During XPS analysis, an Al k_α X-ray beam was adopted as the excitation source and the vacuum pressure of the instrument chamber was 1×10^{-7} Pa as read on the panel. Measured spectra were decomposed into Gaussian components by a least-square fitting method. Binding energy was calibrated with reference to C1s peak (285.0 eV).

2.3 Catalytic tests.

The catalytic activity of the Cu-CeO_2 composite nanoparticles with 50 mg heated in situ for CO oxidation was evaluated at atmospheric pressure in a glass tubular reactor. The total flow rate of the reaction gas was flow of 30 L h^{-1} g^{-1}, with a 1% CO and fresh air balanced composition from air generator. The catalyst was heated to the desired reaction temperature at a rate of 2 ^oC min^{-1} and then kept there for 50 min until the catalytic reaction reached a steady state. The composition of the gas exiting the reactor was monitored by online gas chromatography (GC 9800). The CO conversion (R_{CO}) was calculated from the change in CO concentrations of the inlet and outlet gases as follow:

$$R_{CO} = (1 - \frac{[CO]_{out}}{[CO]_{in}}) \times 100\% \qquad (1)$$

where, $[CO]_{in}$ and $[CO]_{out}$ stand for the CO concentrations in the feed gas and effluent gas, respectively. H_2-TPR experiments were carried out by a thermal conductivity detector on 50 mg samples in 80% (molar) argon and 20% (molar) hydrogen gas mixture, allowing flowing at a rate of 100 mL min^{-1} with a temperature ramp rate of 10 ^oC min^{-1}.

3. Results and discussion

The XRD patterns of Cu-CeO_2 composites (with a Cu^{2+}/Ce^{3+} molar ratio of 0, 0.05, 0.10, 0.20, 0.30 and 0.40, respectively) are presented in Fig. 1. All the samples are the random orientation with good crystallinity. Fig. 1 shows the X-ray diffraction (XRD) patterns with well-developed reflections of the CeO_2, Cu-CeO_2 and Cu-CuO-CeO_2 composite, respectively. As shown in Fig. 1, the effects of the different molar ratios of Cu on the crystallographic structure of CeO_2 can not be observed. Fig. 1 shows a decrease of crystallinity in the

Cu-CeO_2 composites in comparison with the pure sample by the decrease in the intensity of CeO_2 peaks when the Cu content increased from 0 to 40.0%. Because of the interference of Cu with CeO_2 lattice, the crystallinity of the Cu-CeO_2 composites was worse than that of pure CeO_2. As shown in Fig. 1(a) and (b), one can see that the diffraction peak positions are matched well the standard data for bulk CeO_2: JCPDS Card No. 81-0792, indicating that the samples are the crystalline cubic phase CeO_2 crystal structure, without any reflections of the byproducts such as Cu or CuO. This finding implies that the Cu atoms most probably occur by substituting Ce atoms in the crystal structure. It can be clearly seen from Fig. 1(c)-(e) that all diffraction peaks can be assigned to the cubic phase of CeO_2 with lattice constants a=5.412 Å (JCPDS No. 81-0792) coexisting with the cubic phase of Cu with the lattice constant a=3.615 Å (JCPDS No. 85-1326). XRD peaks of CuO are not detected in the samples with low Cu content, however, Fig. 1(f) shows the X-ray diffraction (XRD) patterns with well-developed reflections of the CeO_2, Cu and CuO (JCPDS Card No. 78-0428), respectively. The lattice constants of the products are presented in Table 1. For all investigated materials, the values of lattice constants of Cu-CeO_2 composite are very close to ICDD values (a=5.412 Å). The table shows that the lattice parameters of the products are slightly decreased with increasing Cu concentration. Theoretically, since the ion radius of Cu^{2+} (0.69 Å) is smaller than that of Ce^{3+} (0.74 Å), the (111) peak of Cu-CeO_2 composite should move to larger angle slightly when compared to that of pure CeO_2 (2θ =28.51º) obtained at the same condition. From Fig. 1(a)-(d), they can be seen that the (111) peak of Cu-CeO_2 composite slightly shifts to a high angle. It implies that the Cu doping most probably occurs by substituting Ce atom in crystal structure. The crystalline grain sizes of

Cu-CeO_2 composites decrease from 14.5 to 6.4 nm when the Cu content increased from 0.0 to 40%. According to the XRD patterns, they can be estimated the proportion of Cu and CeO_2 phases, which is calculated as

$$f(\beta) = \frac{I_{Cu}}{I_{Cu} + I_{CeO_2} + I_{CuO}}$$

where $f(\beta)$ is the fraction of Cu, CeO2, or CuO phase, I_{Cu}, I_{CeO_2} and I_{CuO} are the intensity of the diffraction of Cu at 2θ=43.3°, CeO_2 at 2θ=28.5°, and CuO at 2θ=36.5°, respectively. The results are shown in Table S1.

The X-ray diffraction analysis of the as-synthesized 30Cu-CeO_2 composite shows a crystalline structure in Fig. 2, and weak diffraction peaks of CuO are seen. The diffraction peaks at 28.47°, 33.11°, 47.48°, 56.30°, 59.07°, 69.44°, 76.56°, 79.03° and 88.31° can be respectively denoted as (111), (200), (220), (311), (222), (400), (331), (420) and (422) reflections of CeO_2, and 43.30°, 50.42°, 74.08° denoted as (111), (200) and (220) reflections of Cu. The *hkl* indexes indicated in the plot correspond to the CeO_2 cubic structure. The application of Scherrer's equation to the (111) plane diffraction peak (2θ =28.47°) of the XRD spectrum yields a crystal size of ~9 nm.

SEM image (Figure S1) revealed that there were various sizes of particles in the Cu-CeO_2 nanoparticles. Most particles are irregular morphology and the large particles were composed of small crystallites. The morphological properties of the Cu-CeO_2 composites are further investigated by TEM. HR-TEM was also used to probe the dispersion of Cu in the Cu-CeO_2 composites. Fig. 3 shows an overview image and illustrates that the particles are partially aggregated but otherwise rather uniform in size and shape. At low Cu content (Fig. 3(a) and (b)), the nanoparticles tend to aggregate. The Cu-CeO_2 composites exhibit a nearly

cubic shape with an average size of 10~25 nm. The particle size, as determined from the TEM image, is obviously by a factor 1.5~2.0 bigger than the apparent crystallite size determined from XRD experiments, because the particles seen in TEM could be composed of smaller primary particles of several nanometers in size. TEM images clearly show that the particle sizes are gradually decreased with increasing Cu concentration, which are in good accordance with the XRD results described above. Fig. 4 shows a representative TEM collected over the 30Cu-CeO_2 nanoparticles. The overview image in Fig. 4(a) at low magnification proves that the sample entirely consists of individual CeO_2 particles. It is clear that the catalyst displays surface agglomeration of nanoparticles with uniform size distribution. To get further insight into the atomic order of the 30Cu-CeO_2 nanoparticles, high-resolution images were recorded. As shown in Fig. 4(b), the HR-TEM image shows the well-developed lattice planes additionally demonstrate the high crystallinity. Each Cu-CeO_2 nanoparticle is well crystallized, with an average particle size of 8~9 nm consistent with the crystallite size obtained by XRD. For 30Cu-CeO_2 nanoparticles, one can observe that Cu particles are epitaxially grown on the CeO_2 support in a number of cases. An example is shown in Fig. 4(c), where a HRTEM image of a partly overlapping Cu particle attached to the CeO_2 support is shown. The most frequently observed reflection with *d* spacing value of 0.314 nm corresponds to crystal lattice plane (111) of CeO_2. The reflection with spacing value of 0.207 nm, attributable to the lattice plane (111) of Cu, can also be identified. The selected area electron diffraction (SAED) pattern displays diffraction rings that are characteristic for crystalline nanoparticles and that match with the cubic CeO_2 structure (Fig. 4(d)).

Nitrogen sorption measurement was applied to determine the surface area of the 30Cu-CeO_2 nanoparticles. Fig. 5 shows the N_2 sorption isotherm of the 30Cu-CeO_2 nanoparticles. Gas sorption measurement indicates at high relative pressures the presence of the macropore network of the powder assembly. The Brunauer–Emmett–Teller (BET) specific surface area of the as-prepared sample was ca. 55.7 m^2g^{-1}. The other Cu-CeO_2 nanoparticles with the different Cu contents show similar specific surface area.

In order to investigate the surface nature of the prepared samples, XPS analysis was also carried out and focused on the sample of Cu-CeO_2 nanoparticles. The Ce 3d core level peak can be confirmed by XPS analysis, as shown in Fig. S2. This spectrum is fully consistent with those reported previously [34]. To rationalize XPS findings, one can state that the presence of Ce^{3+} is a result of oxygen vacancies and this effect is enhanced in nanoparticles because a larger fraction of the atoms are on the surface as the particle size is reduced and the surface atoms have reduced coordination [1]. The oxygen vacancies lead to the transformation $Ce^{4+}\leftrightarrow Ce^{3+}$, a key issue in the redox capability of CO. From Fig. S2, one can find that the ratio of Ce^{4+}/Ce^{3+} is 1.20, 1.24, 1.39, and 1.34 for CeO_2, 10-$CuCeO_2$, 30Cu-CeO_2, and 40Cu-CeO_2 nanoparticles, respectively. It is obvious that Cu-CeO_2 nanoparticles show an increased ratio of Ce^{4+}/Ce^{3+}. As an excellent catalytic material, CeO_2 has a strong oxygen storage and release capacity via the redox shift between Ce^{4+} and Ce^{3+} under oxidizing and reducing conditions, respectively. The Ce^{4+} percentage of 30Cu-CeO_2 nanoparticles reaches the highest value, indicating the highest redox capacity [35]. The XPS results (Fig. S3) illustrate more oxygen vacancy species in the Cu-CeO_2 nanoparticles. The ratio of oxygen vacancies and hydroxyl groups to $O_{lattice}$ of Cu-CeO_2 nanoparticles is 0.13,

0.65, 0.89, and 0.77 for CeO_2, 10Cu-CeO_2, 30Cu-CeO_2, and 40Cu-CeO_2 nanoparticles, respectively. The ratio is obviously increased, indicating that the content of surface oxygen vacancy and hydroxyl group is increased by composing suitable amounts of Cu. However, the surface oxygen vacancy contents would be decreased with further increase the copper contents due to the formation of copper oxide (CuO) on the surface of nanoparticles. For the quantitative analysis of peak positions, line widths, and relative areas of the Cu^0 species, the raw XPS spectra of 30Cu-CeO_2 nanoparticles were fitted to Gaussian–Lorentzian functions using CASAXPS software (Figure S4). The XPS spectra for Cu were simple and easily fitted to Cu^0 species, indicating little oxidation of the Cu nanoparticles.

To evaluate the potential applicability in catalytic activity for CO oxidation, the catalytic performances of the Cu-CeO_2 composite catalysts in CO oxidation are evaluated under a reaction stream with a gas composition of 1.0 vol% CO balanced by fresh air with 20 vol% O_2. The results are shown in Fig. 6, where the CO conversion is reported as a function of temperature. It can be seen that the activity of Cu-CeO_2 composite catalysts is greatly enhanced after doping of the Cu, except 5Cu-CeO_2 composite catalyst. Among the Cu-CeO_2 composite catalysts with various copper contents, the 30Cu-CeO_2 nanoparticles exhibit the highest catalytic activity at the lowest temperature, as well as the excellent redox capability at the lowest temperature. The light-off temperature (temperature of 50% conversion, T_{50}) decreases by 97 °C (from 212 °C to 115 °C) after doping the 30% Cu. Complete conversion of CO is achieved at 180 °C over the 30Cu-CeO_2 nanoparticles. In contrast, 40Cu-CeO_2 nanoparticles show a much lower activity. The T_{50} is 125 °C, which is 10 °C higher than that of 30Cu-CeO_2 nanoparticles.

The stability of the Cu-CeO_2 composite catalysts is examined under the same reaction conditions: 1 vol % CO in air and atmosphere pressure flow of 30 L h^{-1} g^{-1}. As shown in Fig. S5, the Cu-CeO_2 composite catalysts undergoes slight deactivation during 20 h on stream. The conversion of CO experiences deactivation between 10% and 15%.

It is well known that the temperature-programmed reduction (TPR) by H_2 has been used extensively to characterize the oxygen reducibility of doped CeO_2. In this paper, TPR was carried out in order to study the reducibility of the materials, which is related to the Cu activation. It is important to point out that the TPR profile of the pure CeO_2 presents two H_2 consumption peaks, one at 528 ^oC, attributed to the reduction of surface oxygen species (capping oxygen), and the other at 820 ^oC, due to the reduction of bulk oxygen [36-38]. However, the as-synthesized 30Cu-CeO_2 composite nanoparticles exhibit a strong reduction peak at 197 ^oC and a weak peak at 528 ^oC, as shown in Fig. 7. The most important feature in Fig. 7 is the decrease in the reduction temperature of surface oxygen species of ceria from 528 ^oC to 197 ^oC. From the reduction pattern, it can be explained the presence of Cu on the CeO_2 surface, which acts as catalyst in the CeO_2 reduction leading to a shift of the H_2 consumption peaks to lower temperatures [39].

CO conversions can be enhanced by the presence of copper at reaction temperatures above 100 °C [40]. Increased activity for CO oxidation of these segregated Cu species is correlated to the ease of reduction or oxygen vacancy formation [41]. The 30Cu-CeO_2 nanoparticles show 100% conversion of CO at 180 °C. This can be ascribed to the fact that CO strongly adsorbs onto more reduced Cu sites of 30Cu-CeO_2, resulting in less active site for adsorbing surface oxygen O_2, which is activated to O_x^- anion radicals rapidly by oxygen

vacancies. The 30Cu-CeO_2 nanoparticles can produce high density of oxygen vacancies, physisorbed and chemisorbed sites for CO, the effect between the cycle transition of Ce^{4+}/Ce^{3+}, which are beneficial to the improvement of the catalytic performance. The catalytic performance for CO oxidation is enhanced obviously after being composited with copper. The 30Cu-CeO_2 nanoparticles show the best activity due to high redox capability and high oxygen vacancy, supported by the H_2-TPR and XPS analyses results. Based on the discussion above, the possible catalytic mechanism on the Cu-CeO_2 nanoparticles is proposed. It is obvious that the ratio of Ce^{4+}/Ce^{3+} and the oxygen vacancy species of Cu-CeO_2 nanoparticles increase by composing suitable amounts of Cu, indicating that copper induces structure defects and oxygen vacancies as well as perform synergistic effect with cerium ions, which are greatly contributed to the CO oxidation performance [36]. On the other hand, the particle sizes of Cu-CeO_2 nanoparticles are gradually decreased with increasing Cu concentration, which increase the surface area. Therefore, the Cu-CeO_2 nanoparticles can not only increase oxygen storage and release capacity, but also increase the surface area of the catalysts, which also favors the efficient oxidation of CO at low temperature.

4. Conclusion

In conclusion, catalytically active Cu-CeO_2 composite nanoparticles with different Cu contents were synthesized by a facile hydrothermal method, and the materials were used for the oxidation of CO. Crystallographic structure, morphology, particle size, and surface area of the Cu-CeO_2 nanoparticles were measured using XRD, TEM, and BET, respectively. The nearly cubic shape of Cu-CeO_2 composites with an average size of 10~25 nm was obtained.

Their crystalline grain sizes decrease from 14.5 to 6.4 nm when the Cu content increases from 0 to 40%. As for catalytic reactivity, Cu-CeO_2 composite nanoparticles show higher reactivities than CeO_2 nanoparticles in CO oxidation. It is found that small copper particles can be composed on CeO_2 and that copper induces the structure defects, oxygen vacancies and surface area, which have a profound influence on the CO oxidation capacity. The catalytic activity of the Cu-CeO_2 composites exhibits Cu content dependence where the best catalytic activity occurs on Cu/CeO_2 atomic ratio of 30%.

Acknowledgements

This work was supported by the National Natural Science Foundation of China (Grant No.51262029), the Key Project of the Department of Education of Yunnan Province (ZD2013006), Program for Excellent Young Talents, Yunnan University (XT412003) and Department of Science and Technology of Yunnan Province via the Key Project for the Science and Technology (Grant No.2011FA001).

References

[1] H. Li, G.F. Wang, F. Zhang, Y. Cai, Y.D. Wang, D. Igor, Surfactant –assisted synthesis of CeO_2 nanoparticles and their application in the wastewater treatment, *RSC Adv*. 2 (2012) 12413–12423.

[2] S. Royer, D. Duprez, Catalytic oxidation of carbon monoxide over transition metal oxide*s*, *ChemCatChem* 3 (2011) 24–65.

[3] A. Hornés, B. Hungría, P. Bera, L. Cámara, M. Fernández-García, A. Martínez-Arias, L. Barrio, M. Estrella, G. Zhou, J.J. Fonseca, J.C. Hanson, J.A. Rodriguez, Inverse

CeO_2/CuO catalyst as an alternative to classical direct configurations for preferential oxidation of CO in hydrogen-rich stream, *J. Am. Chem. Soc*. 132 (2010) 34–35.

[4] D. Mrabet, A. Abassi, R. Cherizol, T.O. Do, One-pot solvothermal synthesis of mixed Cu-Ce-O-x nanocatalysts and their catalytic activity for low temperature CO oxidation, *Appl. Catal. A* 447–448 (2012) 60–66.

[5] Z.Y. Pu, X.S. Liu, A.P. Jia, Y.L. Xie, J.Q. Lu, M.F. Luo, Enhanced activity for CO oxidation over Pr- and Cu-doped CeO_2 catalysts: effect of oxygen vacancies, *J. Phys. Chem. C* 112 (2008) 15045–15051.

[6] J.H. Fang, Z.Y. Cao, D.S. Zhang, X. Shen, W.Z. Ding, L.Y. Shi, Preparation and CO conversion activity of ceria nanotubes by carbon nanotubes templating method, *J. Rare Earth* 26 (2008) 153–157.

[7] Z.L. Wu, M.J. Li, S.H. Overbury, On the structure dependence of CO oxidation over CeO_2 nanocrystals with well-defined surface planes, *J. Catal*. 285 (2012) 61–73.

[8] K.S. Lin, S. Chowdhury, Synthesis, characterization, and application of 1-D cerium oxide nanomaterials: a review, *Int. J. Mol. Sci*. 11 (2010) 3226–3251.

[9] Tana, M.L. Zhang, J. Li, H. J. Li, Y. Li, W.J. Shen, Morphology-dependent redox and catalytic properties of CeO_2 nanostructures: nanowires, nanorods and nanoparticles, *Catal. Today* 148 (2009) 179–183.

[10] D.S. Zhang, C.S. Pan, L.Y. Shi, J.H. Fang. Template-free synthesis, controlled conversion, and CO oxidation properties of CeO_2 nanorods, nanotubes, nanowires, and nanocubes, *Eur. J. Inorg. Chem*. (2008) 2429–2436.

[11] K.B. Zhou, X. Wang, X.M. Sun, Q. Peng, Y.D. Li, Enhanced catalytic activity of ceria

nanorods from well-defined reactive crystal planes, *J. Catal*. 229 (2005) 206–212.

[12] H.X. Mai, L.D. Sun, Y.W. Zhang, R. Si, W. Feng, H.P. Zhang, H.C. Liu, C.H. Yan, Shape-selective synthesis and oxygen storage behavior of ceria nanopolyhedra, nanorods, and nanocubes, *J. Phys. Chem. B* 109 (2005) 24380–24385.

[13] C. M. Ho, J.C. Yu, T. Kwong, A.C. Mak, S. Lai, Morphology-controllable synthesis of mesoporous CeO_2 nano-and microstructures, *Chem. Mater.* 17 (2005) 4514–4522.

[14] Y. Jiao, F.F. Wang, X.M. Ma, Q.H. Tang, K. Wang, Y.M. Guo, L. Yang, Facile one-step synthesis of porous ceria hollow nanospheres for low temperature CO oxidation, *Micropor. Mesopor. Mater*. 176 (2013) 1–7.

[15] W.H. Shen, X.P. Dong, Y.F. Zhu, H.R. Chen, J.L. Shi, Mesoporous CeO_2 and CuO-loaded mesoporous CeO_2: Synthesis, characterization, and CO catalytic oxidation property,*Micropor. Mesopor. Mater*. 85 (2005) 157–162.

[16] A. Valentini, N.L.V. Carreño, L.F.D. Probst, A. Barison, A.G. Ferreira, E.R. Leite, E. Longo, Ni:CeO_2 nanocomposite catalysts prepared by polymeric precursor method, *Appl. Catal. A* 310 (2006) 174–182.

[17] M.F. Camellone, S. Fabris, Reaction mechanisms for the CO oxidation on Au/CeO_2 catalysts: Activity of substitutional Au^{3+}/Au^{+} cations and deactivation of supported Au^{+} adatoms, *J. Am. Chem. Soc*. 131 (2009) 10473–10483.

[18] X.J. Du, D.S. Zhang, L.Y. Shi, R.H Gao, J.P. Zhang, Morphology dependence of catalytic properties of Ni/CeO_2 nanostructures for carbon dioxide reforming of methane, *J. Phys. Chem. C* 116 (2012) 10009−10016.

[19] T.Y. Li, G.L. Xiang, J. Zhuang, X. Wang, Enhanced catalytic performance of

assembled ceria necklace nanowires by Ni doping, *Chem*. *Commun*. 47 (2011) 6060–6062.

[20] F. Mariño, C. Descorme, D. Duprez, Noble metal catalysts for the preferential oxidation of carbon monoxide in the presence of hydrogen (PROX), *Appl*. *Catal*. *B* 54 (2004) 59–66.

[21] C.N. Costa, S.Y. Christou, G. Georgiou, A.M. Efstathiou, Mathematical modeling of the oxygen storage capacity phenomenon studied by CO pulse transient experiments over Pd/CeO_2 catalyst, *J*. *Catal*. 219 (2003) 259–272.

[22] P.G. Harrison, I.K. Ball, W. Azalee, W. Daniell, D. Goldfarb, Nature and surface redox properties of copper(II)-promoted cerium(IV) oxide CO-oxidation catalysts，*Chem*. *Mater*. 12 (2000) 3715–3725.

[23] S. Hočevar, U.O. Krasovec, B. Orel, A.S. Arico, H. Kim, CWO of phenol on two differently prepared $CuO\text{-}CeO_2$ catalysts, *Appl*. *Catal*. *B* 28 (2000) 113–125.

[24] P.O. Larsson, A. Andersson, Oxides of copper, ceria promoted copper, manganese and copper manganese on Al_2O_3 for the combustion of CO, ethyl acetate and ethanol, *Appl*. *Catal*. *B* 24 (2000) 175–192.

[25] M.F. Luo, J.M. Ma, J.Q. Lu, Y.P. Song, Y.J. Wang, High-surface area $CuO\text{-}CeO_2$ catalysts prepared by a surfactant-templated method for low-temperature CO oxidation, *J*. *Catal*. 246 (2007) 52–59.

[26] T. Caputo, L. Lisi, R. Pirone, G. Russo, On the role of redox properties of CuO/CeO_2 catalysts in the preferential oxidation of CO in H_2-rich gases, *Appl*. *Catal*. *A* 348 (2008) 42–53.

[27] G. Marbán, I. Lopez, T. Valdes-Solıs, Preferential oxidation of CO by CuO_x/CeO_2 nanocatalysts prepared by SACOP. Mechanisms of deactivation under the reactant stream, *Appl*. *Catal*. *A* 361 (2009) 160–169.

[28] P.V. Snytnikov, M.M. Popova Y. Menc, E.V. Rebrov, G. Kolb, V. Hessel, J.C. Schouten, V.A. Sobyanin, Preferential CO oxidation over a copper–cerium oxide catalyst in a microchannel reactor, *Appl*. *Catal*. *A* 350 (2008) 53–62.

[29] V.P. Pakharukova, E.M. Moroz, V.V. Kriventsov, D.A. Zyuzin, G.R. Kosmambetova, P.E. Strizhak, Copper–cerium oxide catalysts supported on monoclinic zirconia: structural features and catalytic behavior in preferential oxidation of carbon monoxide in hydrogen excess, *Appl*. *Catal*. *A* 365 (2009) 159–164.

[30] L. Kundakovic, M. Flytzani-Stephanopoulos, Cu- and Ag-modified cerium oxide catalysts for methane oxidation, *J*. *Catal*. 179 (1998) 203–221.

[31] J. Han, H.J. Kim, S. Yoon, H. Lee, Shape effect of ceria in Cu/ceria catalysts for preferential CO oxidation, *J*. *Mole*. *Catal*. *A* 335 (2011) 82–88.

[32] S.M. Zhang, W.P. Huang, X.H. Qiu, B.Q. Li, X.C. Zheng, S.H. Wu, Comparative study on catalytic properties for low-temperature CO oxidation of Cu/CeO_2 and CuO/CeO_2 prepared via solvated metal atom impregnation and conventional impregnation, *Catal*. *Lett*. 80 (2002) 41–46.

[33] A. Martínez-Arias, D. Gamarra, M. Fernández-García, X.Q. Wang, J.C. Hanson, J.A. Rodriguez, Comparative study on redox properties of nanosized CeO_2 and CuO/CeO_2 under CO/O_2, *J*. *Catal*. 240 (2006) 1–7.

[34] S. Tsunekawa, T. Fukuda, A. Kasuya, X-ray photoelectron spectroscopy of

monodisperse CeO_2 nanoparticles, *Surf. Sci*. 457 (2000) L437–L440.

[35] D.S. Zhang, Y.L. Qian, L.Y. Shi, H.L. Mai, R.H. Gao, J.P. Zhang, W.J. Yu, W.G. Cao, Cu-doped CeO_2 spheres: synthesis, characterization, and catalytic activity, *Catal. Commun*. 26 (2012) 164–168.

[36] H.C. Yao, Y.F.Y. Yao, Ceria in automotive exhaust catalysts: I. Oxygen storage, *J. Catal*. 86 (1984) 254–265.

[37] S.B. Wang, G.Q. Lu, Role of CeO_2 in Ni/CeO_2-Al_2O_3 catalysts for carbon dioxide reforming of methane, *Appl. Catal. B* 19 (1998) 267–277.

[38] J. Barrault, A. Alouche, V. PaulBoncour, L. Hilaire, A.P. Guegan, Influence of the support on the catalytic properties of nickel/ceria in carbon monoxide and benzene hydrogenation, *Appl. Catal*. 46 (1989) 269–279.

[39] G.R. Rao, J. Kašpar, S. Meriani, R.D. Monte, M. Graziani, NO decomposition over partially reduced metallized CeO_2-ZrO_2 solid solutions, *Catal. Lett*. 24 (1994) 107–112.

[40] S. Varghese, M.G. Cutrufello, E. Rombi, C. Cannas, R. Monaci, I. Ferino, CO oxidation and preferential oxidation of CO in the presence of hydrogen over SBA-15-templated CuO-Co_3O_4 catalysts, *Appl. Catal. A* 443–444 (2012) 161–170.

[41] C.S. Polster, H. Nair, C.D. Baertsch, Study of active sites and mechanism responsible for highly selective CO oxidation in H_2 rich atmospheres on a mixed Cu and Ce oxide catalyst, *J. Catal*. 266 (2009) 308–319.

Captions of Figures

Figure 1 X-ray diffraction analysis of Cu-CeO_2 composite nanoparticles with the different Cu contents from 0 to 40%.

Figure 2 XRD pattern of as-prepared 30Cu-CeO_2 composite nanoparticles.

Figure 3 TEM images of Cu-CeO_2 composite nanoparticles with the different Cu contents: (a) CeO_2, (b) 5Cu-CeO_2, (c) 20Cu-CeO_2, and (d) 40Cu-CeO_2, respectively.

Figure 4 (a) TEM image, (b) HRTEM image, (c) high resolution lattice image, showing well-defined nano-crystalline regions of Cu and CeO_2, and (d) selected area electron diffraction of 30Cu-CeO_2 composite nanoparticles.

Figure 5 Nitrogen adsorption/desorption isotherms of 30Cu-CeO_2 composite nanoparticles.

Figure 6 (a) CO conversion rate as a function of the reaction temperature for various Cu–CeO_2 catalysts, (b) CO oxidation activity on various Cu–CeO_2 catalysts at various reaction temperatures.

Figure 7 H_2-TPR profile of as-prepared 30Cu-CeO_2 composite nanoparticles.

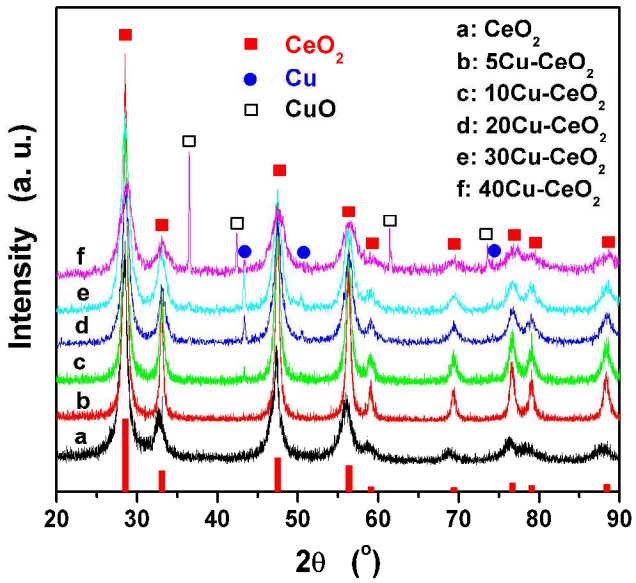

Figure 1

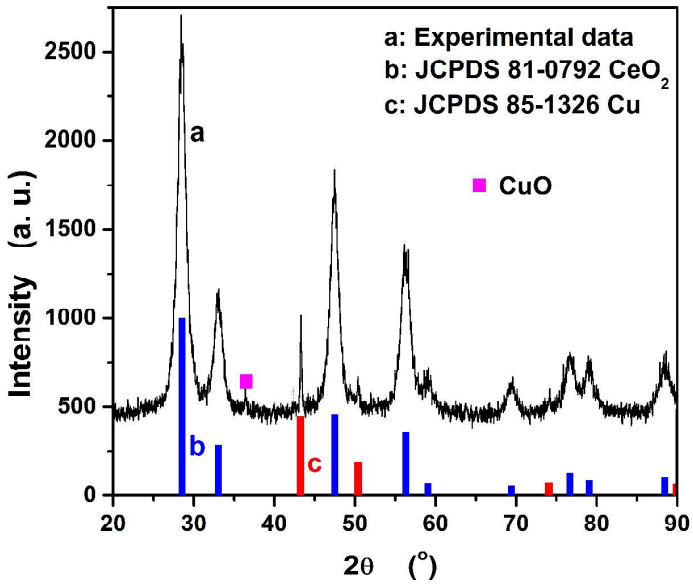

Figure 2

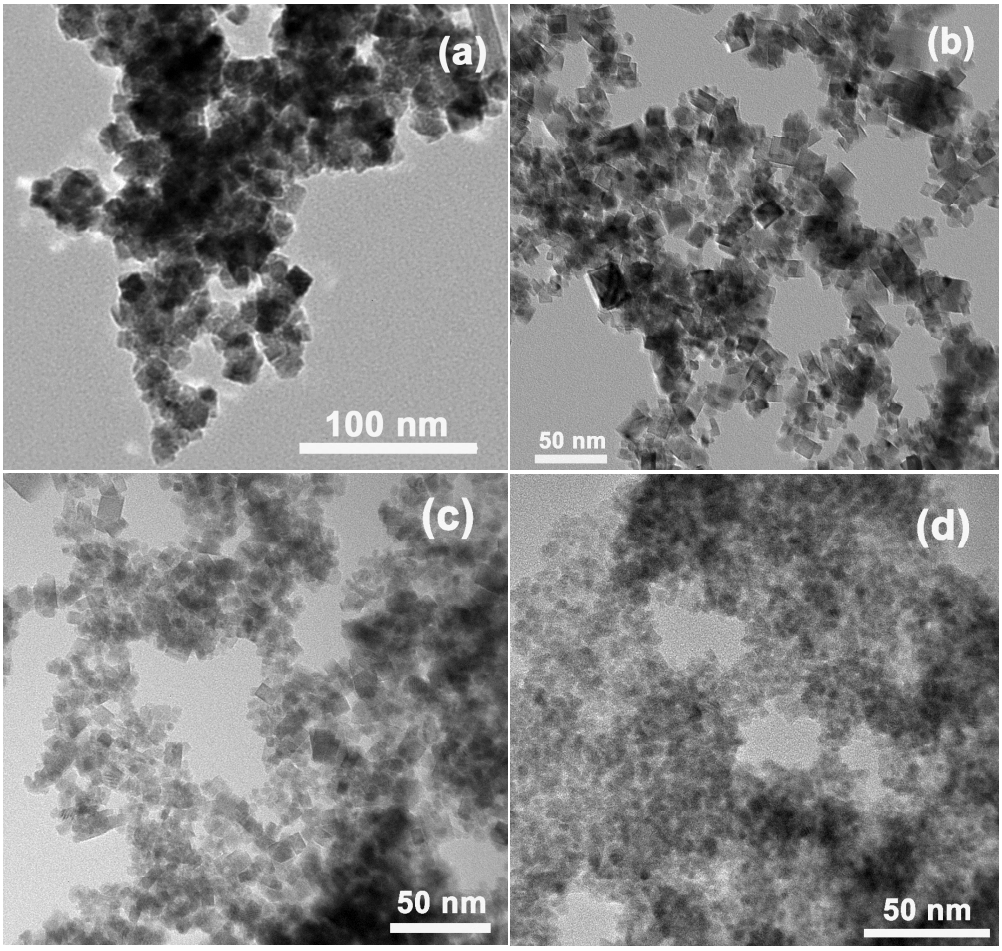

Figure 3

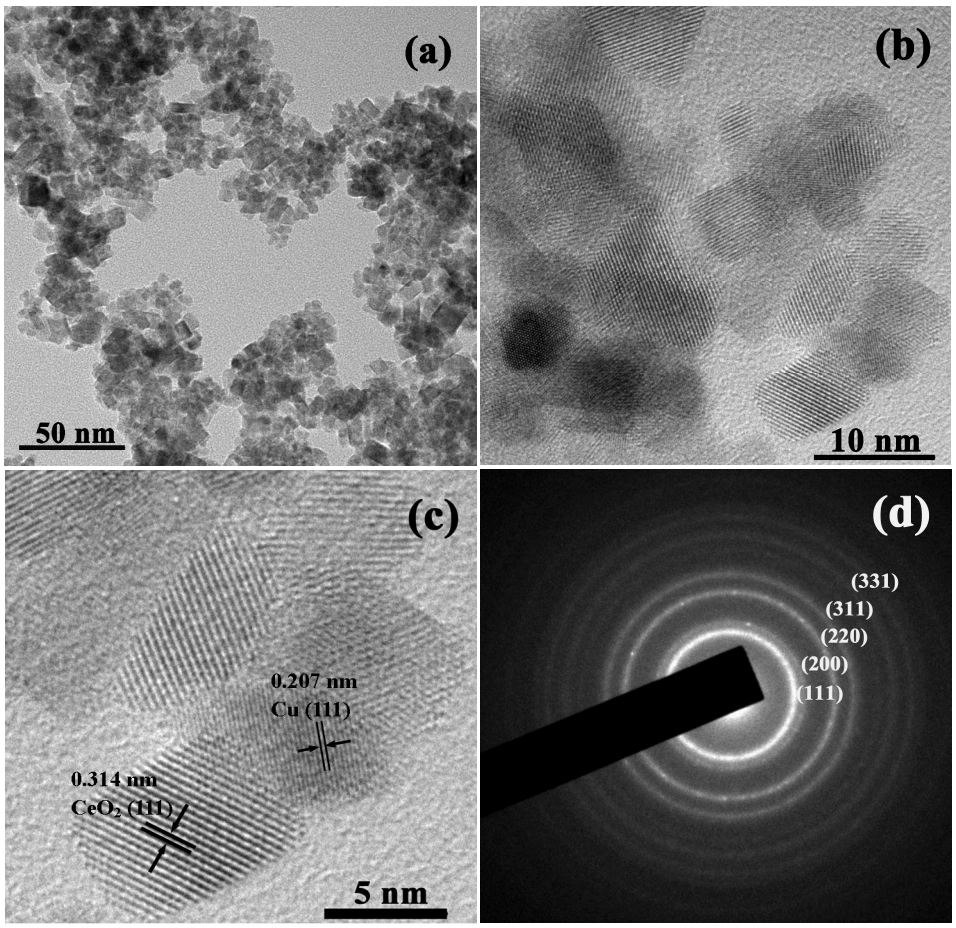

Figure 4

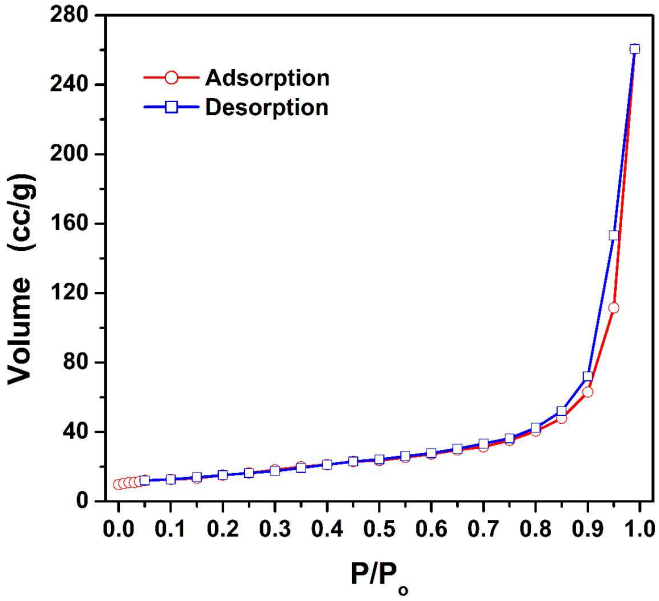

Figure 5

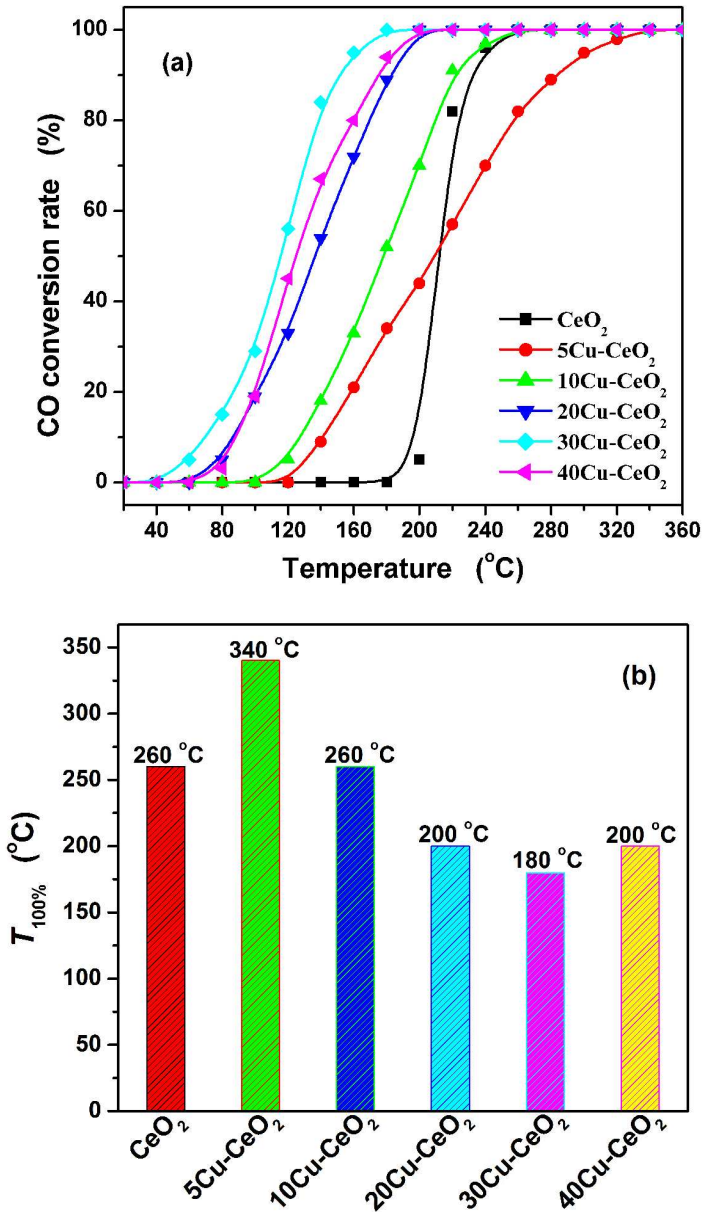

Figure 6

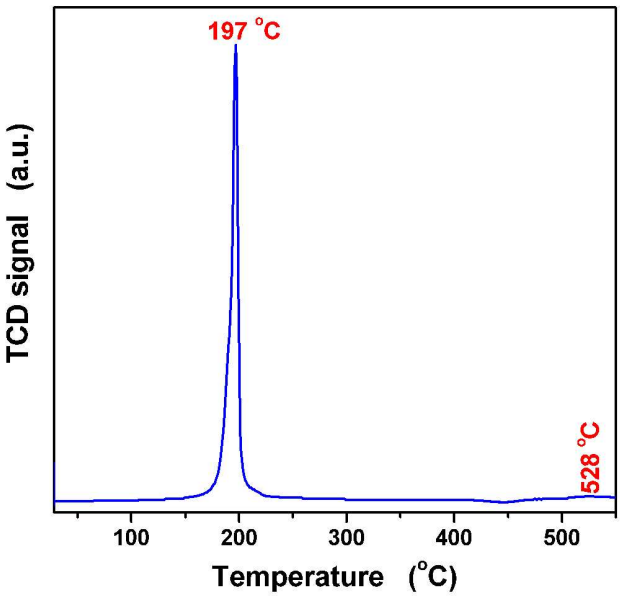

Figure 7

Table 1 The lattice constants and Average crystallite size of Cu-CeO_2 composite nanoparticles.

Average lattice constant †	Cu-CeO_2 composite nanoparticles						
	JCPDS 81-0792	0%Cu	5%Cu	10%Cu	20%Cu	30%Cu	40%Cu
a (Å)	5.412	5.439	5.422	5.419	5.418	5.415	5.409
Average crystallite size § (nm)	—	14.5	13.5	10.4	9.1	8.9	6.4

† The average lattice constants were calculated using Jade5 software from peak locations ((111), (200), (220), (311), (222), and (400) reflections based on the experimental data). JCPDS 81-0792, System: cubic, Lattice: face-centered, Space group: $Fm\bar{3}m$ (225).

§ The crystallite size *D* is deduced from the (111) peak width.